Structural and Morphological Analysis of the First Alloy/Dealloy of a Bulk Si−Li System at Elevated Temperature

Matthew J. Lefler, Junghoon Yeom, Christopher Rudolf, Rachel E. Carter, and Corey T. Love*

Read Online

ACCESS | 📊 Metrics & More | 📖 Article Recommendations | 🆂 Supporting Information

ABSTRACT: There have been tremendous improvements in the field of Si electrode materials, either by nanoscale or composite routes, and though silicon-containing carbon electrode materials have begun to penetrate the marketplace, the commercial capacities achieved by these cells still fall short of the promise of high capacity Si electrodes. Enabling a cheaper feedstock of Si in the bulk form would make this technology more accessible, though there are many challenges that must be overcome. Whereas other methods utilize nanomaterials and composites to overcome volume expansion and pulverization of a Si electrode, this study explores a thermal route to enable the use of carbon-free bulk Si. To accomplish this, a modified Swagelok cell has been constructed to accommodate high temperatures, corrosive molten salt electrolytes, and a molten lithium electrode to study lithiation of a bulk Si wafer at 250 °C. Scanning electron microscopy, X-ray diffraction, and microcomputed tomography were used to examine morphological and structural changes within the Si upon lithiation and delithiation. It was discovered that semiordered Li_xSi phases were formed upon lithiation in molten LiTFSI electrolyte at 250 °C, and the higher temperature does not completely mitigate pulverization of the bulk Si electrode.
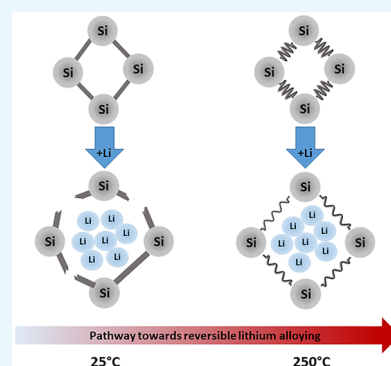
INTRODUCTION

The convenience and practicality of portable energy systems has made lithium-ion batteries (LIBs) ubiquitous in the field of energy storage. However, our energy demands (longer-lasting cell phone batteries, greater range for electric vehicles, more efficient storage for alternative energy sources, etc.) are growing beyond the capabilities of current technology. The graphite electrode in these systems delivers a theoretical lithium storage capacity of 372 mAh/$g_{graphite}$,[1,2] and though state-of-the-art electrodes now include carbon composite materials, the capacity limitations of graphite in these systems greatly restrict the energy storage abilities. Silicon has long been of interest to replace the capacity-limiting graphite electrode[3,4] due in large part to its high natural abundance but also because of its order-of-magnitude larger lithium storage capacity of 3579 mAh/g based on practical lithium alloying to the $Li_{15}Si_4$ phase.[2,5,6]

Preliminary studies of the Li−Si system utilized prelithiated Si alloys, often fabricated via a high-temperature annealing process, and the electrochemical dealloying of these lithium silicides was observed at temperatures much greater than that of this study.[3,4,7] At the risk of oversimplifying these studies, delithiating Li_xSi alloys at 415 °C in molten halide eutectic electrolytes results in four equilibrium alloy phases such that dealloying progresses as follows: $Li_{22}Si_5 \rightarrow Li_{13}Si_4 \rightarrow Li_7Si_3 \rightarrow Li_{12}Si_7$ at equilibrium voltages between 2−44 mV, 44−158 mV, 158−288 mV, and 288−332 mV relative to lithium, respectively.[7]

At room temperature, electrochemical alloying of Li and Si has been reported to result in an amorphous Li_xSi phase instead of the alloys previously mentioned because the formation of these equilibrium intermetallic compounds is kinetically less favorable at lower temperatures. Thus, room-temperature studies of Li−Si alloying have reported a relatively flat single voltage plateau of ∼100 mV during the alloying process for the formation of the amorphous Li_xSi phase and a similarly singular voltage plateau during dealloying at approximately 450 mV.[8]

However, it must be noted that in the process of alloying with Li the Si lattice structure must expand to accommodate these interactions, thus causing significant volume changes and severely damaging the structural integrity of the Si material.[5,6,8−11] Generally speaking, when an amorphous lithiated silicon (a-Li_xSi) layer is formed on the Si surface during lithiation, it is under compressive stress because of a volume expansion constraint generated by the underlying substrate. However, actual stress development and morphological evolution of Si electrodes during the initial lithiation step depend on the electrode geometry and crystallinity. In single-

crystal Si wafers, it has been reported that lithiation alone does not induce cracks in the a-Li$_x$Si layer, and instead the compressive stress in the a-Li$_x$Si layer results in the substrate bowing[12] and/or buckling.[13] In those experiments, cracks appeared only after the first delithiation step[13] or multiple lithiation/delithiation cycles.[9]

This volume expansion during alloying/dealloying and the subsequent pulverization greatly diminish the lithium storage capabilities of the material in the following ways: (1) the active silicon particles fragment and lose electrical connectivity, leading to "dead" Si, and (2) as the Si breaks apart, fresh Si is exposed, resulting in a continuous depletion of the Li inventory due to the constant formation of new solid electrolyte interfaces (SEIs).[8,10,14−16] To mitigate these problems, many studies have focused on optimizing the Si electrode structures by utilizing nanostructured Si, such as nanoparticles, nanotubes, and nanowires,[8,11,15] forming a composite, usually with carbon,[5,10,17,18] or incorporating electrode/electrolyte additives, such as polymeric binders of Si nanoparticles.[14,18] Each of these methods requires extensive processing or extra materials, which increases the price per kWh and ultimately makes the resulting batteries functional but challenging to produce on a commercial scale.[9]

Although there have been tremendous improvements to this technology by using these nanoscale and composite routes, this study aims to supplement this field by enabling a cheaper feedstock of Si in the bulk form. As a bulk material, Si is more accessible because no expensive processing is required, Whereas others have taken the synthetic route, altering the material to overcome the volume expansion, this study explores the possibility of using a thermal route to enable the use of the bulk Si. To accomplish this, we have developed a Swagelok cell able to withstand high temperatures of at least 250 °C that utilize a molten salt electrolyte. In this higher-temperature environment, the interatomic bonding of the Si material is assumed to be more elastic,[19] and the increased ductility of these bonds can then be leveraged to diminish pulverization, thus extending the cycle life of the silicon electrode. This study aims to understand the Li and Si alloying and dealloying reaction processes and the resulting mechanical fracture that occurs under these elevated temperature conditions utilizing SEM and micro-CT analytical techniques.

■ EXPERIMENTAL SECTION

2.1. Preparation of the Si Wafer. Si electrodes (P-type, ⟨100⟩, 0.001−0.005 Ohm-cm, single-sided, 0.5 mm thick) were prepared using a laser milling system (Oxford) to dice a larger wafer into 1 cm × 1 cm square coupons. These electrode coupons were subjected to a buffered oxide etch (J.T. Baker, buffered oxide etch (6:1, NH$_4$F/HF), CMOS for microelectronic use) to remove a native oxide layer immediately prior to being placed into an Ar-filled glovebox.

2.2. Preparation of the Swagelok Cell. The Swagelok cell described here was adapted from the cell described in Muñoz-Rojas et al.[20] A Swagelok 316 stainless steel tube fitting (union, 5/8" tube OD) was hollowed out such that there was a single smooth bore of 5/8" diameter. A 5/8" diameter steel rod (also 316 stainless steel) was secured into one side of the fitting, to be utilized as the electrical connection for the Li electrode. A second 316 stainless steel rod (0.59" diameter) was wrapped in PTFE tape to ensure electrical isolation from the Swagelok cell casing and maintain the inert atmosphere inside the cell when assembled in an Ar-filled glovebox. Inside

the glovebox, a corrosion-resistant compression spring (0.5" long, 0.48" OD, 302 stainless steel, McMaster-Carr item 9002T18) was placed in the cell on top of the steel rod, followed by a coin cell spacer (302 stainless steel, 15 mm diameter, MTI Corporation). Lithium ribbon (Sigma-Aldrich, 0.38 mm thickness, 99.9% trace metals basis) was cleaned with a brush to remove any surface contamination such as oxides or nitrides, and a 1/2" punch was used to create the Li chip that was placed on top of the steel spacer. Due to the operating temperature of these experiments being above the melting point of lithium (m.p. 180 °C), high-volume particle-filtering wire cloth (316 stainless steel, 72 × 72 mesh size, McMaster-Carr item 9230T66) was punched out to a 5/8" diameter and placed on top of the Li chip. The purpose of this wire mesh was to take advantage of capillary forces to prevent the molten lithium from penetrating through the separators and instigating a short circuit, as the liquid lithium will instead be trapped within the pores of the mesh. A slightly oversized Whatman 934-AH glass fiber separator (1.5 μm pore size) was added and tamped down onto the assembly, and ∼0.60 g of electrolyte powder, either lithium bis(fluorosulfonyl)imide (LiFSI, Nippon Shokubai Co., Ltd., 99%) or lithium bis-(trifluoromethanesulfonyl)imide (LiTFSI, Sigma-Aldrich, 99.95% trace metals), was added to the cell. Another Whatman 934-AH separator was arranged on top of the electrolyte, and the components were compacted into the cell. The prepared 1 cm × 1 cm Si coupon was placed in the center of the top separator with the polished side in contact with the separator. The cell was completed by securing the Swagelok fitting around the PTFE-wrapped stainless steel rod that served as the Si electrode contact, while a clamp provided pressure to both sides of the cell (i.e., compression of the interior spring was essential to ensure good electrical contact as the electrolyte melted). A diagram of the completed cell and interior components can be seen in Figure 1. Note that the orientation of the cell in Figure 1 is upside down, a point that will be discussed in the next section.

2.3. Experimental Conditions. The cell was removed from the glovebox and prepared for heating. Copper wires, to be used as electrical leads and shielded with a fiberglass sleeve to prevent excessive oxidation, were attached to either end of
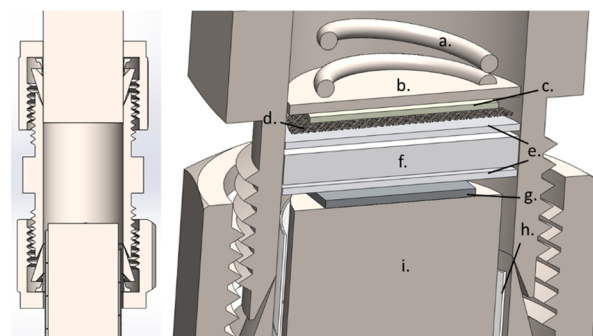
Figure 1. Construction of the high-temperature experimental cell. A modified version of the Swagelok cell used with permission from Muñoz-Rojas, D., et al. Development and implementation of a high temperature electrochemical cell for lithium batteries. *Electrochem. Commun.* **2007**, *9* (4), 708−712. Cell components are as follows: (a) 302 stainless steel spring (30.42 lbs/in), (b) 302 stainless steel spacer, (c) Li chip, (d) stainless steel mesh, (e) glass fiber separator, (f) electrolyte powder, (g) bulk Si wafer (buffered oxide etched), (h) Teflon tape shroud, and (i) 316 stainless steel current collector.

the cell with hose clamps, and the cell was placed in a muffle furnace (Barnstead Thermolyne 47900). When placed in the oven, the cell was oriented such that the Si side was the bottom, as shown in Figure 1. The oven was rapidly brought to 100 °C and allowed to equilibrate at this temperature for approximately 1 h. After equilibration, the temperature of the muffle furnace was increased at a ramp of 2 °C/min up to 250 °C, where the temperature was held constant throughout the rest of the experiment. The Swagelok cell was allowed to heat and equilibrate for a total of 2 h, during which time the open-circuit voltage (OCV) was measured using an Ametek PARSTAT MC Multichannel Potentiostat chassis with a PMC-1000 unit and VersaStudio software. After 2 h, a current of −0.4 mA (i.e., a current density of 0.4 mA/cm²$_{Si}$) was applied to the cell, resulting in the movement of lithium from the Li electrode into the Si electrode in the first "alloying" step. Dealloying, when applicable, was performed at +0.4 mA.

Three conditions were studied here: (1) *Partial alloy*, in which the alloying stage was terminated at a time limit of 8 × 10⁴ s (approximately 22 h), determined to be less than or equal to half of the average time required for the cell to reach the lower voltage limit. (2) *Full alloy*, where the cell was allowed to continue the alloying stage until a lower voltage cutoff of 10 mV was achieved. (3) *Alloy/dealloy*, which represents a full first cycle of the Li vs Si system for an alloy step to a lower voltage limit of 10 mV and a dealloy step to an upper voltage limit of 1.2 V.

For cyclic voltammetry, the cell was first brought up to temperature (250 °C) and held for approximately 2 h before the sweep began. The scan began near the OCV at 2.5 V and was swept toward lower potentials at a rate of 0.05 mV/s before cycling between 0.01 and 1.2 V vs Li/Li⁺ at the same sweep rate. The Ametek PARSTAT system described above was also used to perform the CV experiments.

2.4. Analysis of Si Electrodes. Post-mortem analysis of the Si electrodes was conducted by cooling the Swagelok cell and removing the Si coupon in the atmosphere. The coupon was carefully washed with a minimal amount of water to remove sections of the separator adhered to the Si surface. Analysis techniques included powder X-ray diffraction (PXRD), performed on a Rigaku instrument with a Cu-rotating anode at a rate of 2.5°/min and a 0.02° step width, and scanning electron microscopy (SEM), using a Thermo Fisher Scientific Quattro ESEM.

Often, preparing post-mortem Si samples for SEM, which involves a water rinse and using methods such as cleaving the coupon to expose cross-sectional views, induces additional stress on the sample, which can lead to the appearance of features that are not caused by experimental conditions; however, sample preparation for micro-CT (computed tomography) analysis is minimal, reducing strain on the sample and allowing for a more accurate view of the fracture development within these coupons without the influence of external stressors. Specifically, CT sample preparation was performed such that the sample was removed from the Swagelok cell in an argon-filled glovebox and hermetically sealed in a thin plastic sample container; thus, the sample was never exposed to the atmosphere or a water rinse. The CT analysis technique scans through the sample in slices, which can then be compiled to create a 3D rendering. Two samples were analyzed with micro-CT to corroborate the results from the SEM, using a lab-scale Zeiss Xradia 520 Versa X-ray microscope (Carl Zeiss X-ray Microscopy). The detection

system consisted of a scintillator coupled to a 16-bit charge-coupled device (CCD) detector.

2.5. Room-Temperature Coin Cell Fabrication and Testing. For comparison with the high-temperature Li vs Si system, 2032 coin cells were fabricated using coin cell can materials from Hohsen Corp. As with the high-temperature cells, a chip of Li (Sigma-Aldrich, 0.38 mm thickness, 99.9% trace metals basis) was punched out of the larger ribbon as one electrode. Approximately 45 μL of electrolyte, 1 M LiPF₆ in EC/DEC (50/50 by volume) (Sigma-Aldrich, battery grade), was dropped onto the Li metal, followed by the separator, the same Whatman 934-AH glass fiber separator that is used in the high-temperature setup. Another 45 μL of electrolyte was pipetted onto the separator for a total of ~90 μL. The Si wafer was then placed on top of the separator, and the cells were sealed using a Hohsen Corp. automated coin cell crimper. Alloying and dealloying were performed on a Maccor 4300 desktop automated battery testing system at 0.4 mA/cm²$_{Si}$ with a time cutoff of 55 h for each step (or a 0.01 V lower voltage cutoff and a 1.2 V upper voltage cutoff) to enable direct comparison between the room-temperature and high-temperature results.

■ RESULTS AND DISCUSSION

3.1. Electrolyte Compatibility and Benefits of a Molten Salt Electrolyte. The elevated temperature of 250 °C employed in this study required special considerations with regard to electrolyte, and it was determined that molten salts with lower melting points would be ideal for this application. The LiFSI and LiTFSI salts were chosen as candidate electrolytes due to having melting points in the desired temperature domain and having been shown to be useful electrolyte components in LIB systems prior to this study, though mainly as electrolyte additives at room temperature.[20,21] These salts, often used as components in ionic liquids (ILs), benefit from wide electrochemical potential windows, extremely low vapor pressures, nonflammability, and thermal stability over a wide range of temperatures, aspects which are characteristic of molten salts.[22−24] Despite their apparent advantages, ILs may suffer from poor ionic conductivity compared to room-temperature electrolytes, often due to their relatively high viscosities.[22,25] These challenges also persist in the use of these liquid salts at high temperatures. Additionally, ILs can be highly corrosive to some materials; for example, LiTFSI was considered as a replacement for LiPF₆ in commercial LIBs, but high concentrations of the TFSI⁻ anion were found to corrode the aluminum current collector.[21]

In this study, it was determined that the 316 stainless steel utilized for the cell body and current collectors was not vulnerable to corrosion from these molten salts, but the internal components of the cell were not as robust. During experimentation, the molten LiFSI became dark brown in color and dissolved the glass fiber separator, thus causing internal shorting. This is likely due to the thermal stability of LiFSI at higher temperatures being highly dependent on the purity of the salt. Ultimately, LiFSI was determined to be incompatible with the internal components used in the setup of the experimental cell, and consequently LiTFSI was used as the electrolyte.

Although the use of LiTFSI was beneficial with regard to the compatibility of electrochemical cell materials, this salt is extremely viscous in its molten state, resulting in the

aforementioned reduced ionic mobility throughout the electrolyte. However, though LiTFSI is an imperfect electrolyte, Muñoz-Rojas et al. provide a precedent for the use of molten LiTFSI in a lithium-based system in the 250 °C temperature domain.[20] Additionally, the melting point of this electrolyte (~236 °C, depending on purity) is close to the operation temperature of the cell, resulting in a much safer system as it is inert at ambient temperature. It is shown in Figure 2 that activation of this cell does not occur until the system is brought up to the desired operating temperature of 250 °C.
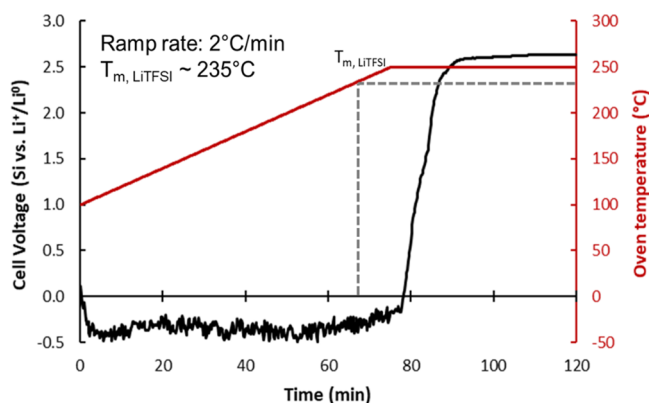
Figure 2. Thermal activation of molten salt electrolyte to produce open-circuit voltage. The onset of thermal activation of the electrochemical cell occurs upon electrolyte melting. Prior to melting, the cell is inactive. These data are an average of five independent identical experiments to reduce noise and give a more accurate representation of cell voltage. The environmental temperature of the Swagelok cell was ramped from 100 to 250 °C@2 °C/min.

3.2. Alloying and Dealloying Results.

The observed voltage for the alloying process that occurs in the intermediate temperature domain of 250 °C studied here is 230 mV ± 15 mV, and the reverse reaction progresses via a two-step dealloying process, with one voltage plateau occurring at ~400 mV and the second at ~550 mV, as seen in Figure 3(a), and as confirmed by differential capacity (dQ/dV) analysis, shown in the SI. In both of these processes, the voltages are

much higher than those observed in the comparable room-temperature (RT) cell, which maintained a voltage between 45 and 50 mV for the majority of the 55 h of alloying (see Figure 3(a)). The RT dealloy revealed a high hysteresis between 200 and 350 mV, and a significant drop in cell voltage after only ~15 h of dealloying indicated the onset of electrical failure. The alloying and dealloying voltages reported here are lower than those previously observed in a comparable system at room temperature,[8,15] though this is likely an effect of the higher current density utilized in these experiments as well as slight differences in experimental setup (e.g., using a crystalline electrode instead of a powder).

Aside from the differences in cell voltage during alloying and dealloying, another distinction between the high-temperature cell and the RT cell in these experiments is the inability of the silicon wafer in the RT cell to fully dealloy due to electronic failure within the cell. The immediate effect of pulverization is on display here, where at RT the crystalline silicon material has essentially destroyed itself by continuing to alloy with lithium until the material loses its integrity; however, at a higher temperature, the system seemingly has a self-imposed alloying limitation that allows for relatively high areal capacity while maintaining the ability to fully dealloy to a 1.2 V cutoff. The idea of placing limits on the degree of alloying to prevent pulverization is not new,[16] but it is usually accomplished via limitations on allowed capacity, which somewhat diminishes the allure of using a high capacity system. In this high-temperature system, though, the capacity is determined by the intrinsic material properties as they relate to cell voltage, as opposed to a set capacity limit.

In the cyclic voltammetry (Figure 3(b)), the first cathodic sweep shows a peak near 1 V, though only in the first cycle. This peak is attributed to the irreversible reaction between the Si electrode and the electrolyte, which helps to form an SEI layer.[26,27] The majority of the cathodic response is observed at low voltages, with the onset of the current occurring at ~230 mV, as would be expected based on the V vs time data. In the anodic sweep (corresponding to the dealloying step), multiple peaks appear, though these occur at voltages slightly higher than expected, closer to 575 mV and 710 mV instead of 400 mV and 550 mV as estimated from the electrochemical data and the dQ/dV analysis. This discrepancy is likely due to the
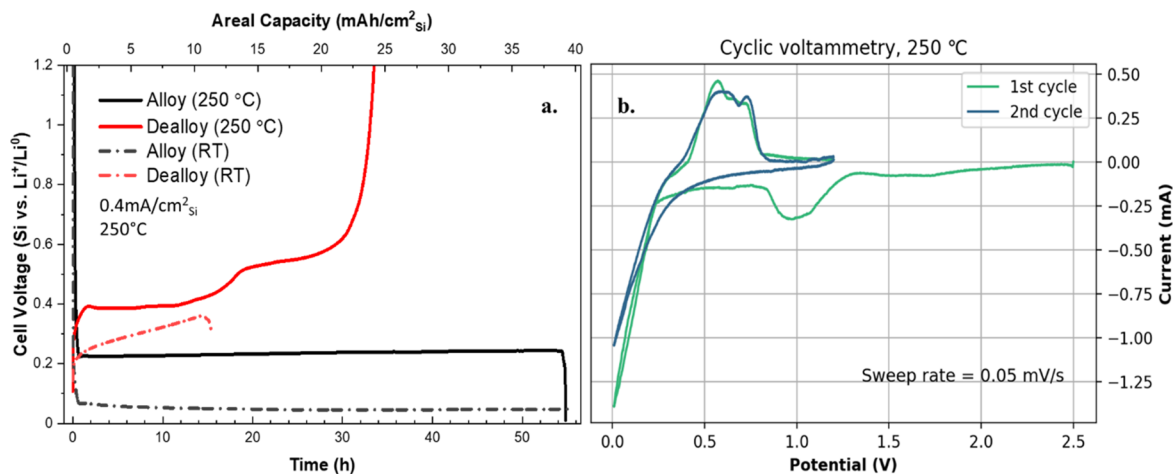
Figure 3. (a) Electrochemical data for the initial Li alloy and dealloy of a bulk silicon coupon. Alloy and dealloy steps were performed with a current density of 0.4 mA/cm² at 250 °C (solid lines) and room temperature (dashed lined). (b) Cyclic voltammetry was performed on the Li vs Si system at 250 °C using a sweep rate of 0.05 mV/s for two cycles.

Figure 4. XRD patterns of a bulk silicon coupon (bottom) and Si electrodes after heating to 250 °C and partial electrochemical alloy (red), full alloy (blue). and alloy/dealloy (green) with lithium.

sweep rate used for CV, which can shift anodic peaks to higher values when using a faster rate.

Room-temperature CV studies of the reaction between Li and Si have shown lithium insertion (cathodic current) to occur at these lower potentials and show behaviors similar to those observed in the literature, depending on the sweep rate.[28,29] In the anodic sweep, room-temperature studies have shown multiple behaviors, again depending on the rate: some studies have shown only one peak, which narrows as the sweep rate decreases,[28] but at very slow rates two peaks can be differentiated in the anodic sweep, corresponding to the formation of various amorphous Li_xSi phases.[29] In these studies, the caveat is that Li insertion into Si anodes is either "sluggish" or requires a very low sweep rate to achieve proper alloying.[28,29] This is not the case in this study, in which a comparatively very high current density is used for alloying and dealloying.

In the electrochemical data, the higher experimental voltages observed in the high-temperature system are likely in part due to the liquid character of the molten salt, which has a higher viscosity compared to more conventional liquid electrolytes, greatly impacting the ion transport properties of the LiFTSI.[22,25,30] In addition to the high viscosity resulting in a reduction in ionic mobility, the Walden rule states that the relationship between viscosity and molar conductivity is inversely proportional;[30] thus, the molten LiTFSI requires higher voltages for the transfer of lithium ions. Additionally, the voltage features present in the dealloying stage suggest the presence of a semicrystalline state at this temperature domain.

X-ray diffraction of the Si electrodes after the electrochemical tests identifies the crystalline phases formed during the alloying and/or dealloying process. The spectra in Figure 4 represent a bulk silicon coupon prior to electrochemical testing, as well as coupons that have undergone the three experimental conditions noted in the Experimental section (partial alloy, full alloy, and alloy/dealloy). These coupons are single-crystal silicon; thus, only the peak which corresponds to the out-of-plane orientation will appear in the diffraction pattern. Since the wafer has an orientation of (100), according to extinction rules,[31] the only expected peak is the (400) reflection, which occurs at $2\Theta = 68.7°$. Typical crystalline silicon peaks at $2\Theta = 28.3°$, $47.0°$, and $55.8°$ representing the (111), (220), and (311) reflections, respectively, are not expected to appear because the diffraction condition is not satisfied. This is true for the two experimental samples that have undergone partial and full alloying. However, in the alloy/

dealloy sample, very broad peaks at these diffraction angles can be observed, indicating that the dealloying process has caused the Si to be broken up into smaller grains that are intermixed with the other phases in the sample. These Si grains, which have a different physical orientation, satisfy the diffracting condition, and the broad nature of these peaks indicates a degree of amorphization of the Si. In addition to the appearance of the broadened (111), (220), and (311) peaks, there is also a sharp peak at $2\Theta = 33.0°$ that appears only in the sample that has been subjected to dealloying. This peak is potentially the forbidden Si (200) reflection,[32] which has been hypothesized to occur upon Si lattice distortion,[33] in this case made visible due to the dealloying process, and further study of this region of the diffraction spectrum may be useful in analyzing core structure defects in the silicon lattice.[34]

Additional peaks of interest in these spectra include those at $32.5°$ and $33.5°$, as well as $38.7°$ and $45.0°$. These four peaks correspond to the spectra of LiTFSI shown in Muñoz-Rojas et al.,[20] and a summary of the major peaks in the LiTFSI spectrum and their approximate relative intensities can be found in Table 1. The larger intensity of the latter two peaks

Table 1. LiTFSI and LiF Powder Diffraction Peaks and Relative Intensities

compound	peak location (2Θ, degrees)	relative intensity (normalized)
LiTFSI[20]	32.25	0.300
	33.75	1.00
	37.50	0.142
	38.50	0.627
	44.75	0.343
LiF (JCPDS 72−1538)	38.70	0.749
	45.00	1.00

also indicates the presence of lithium fluoride (LiF), an inorganic compound that is assumed to have formed on the Si electrode as a component of the solid-electrolyte interphase (SEI). Between the two LiF peaks, there are a number of unidentified features, specifically the two peaks in the spectrum of the full alloy sample at $2\Theta = 41.3°$ and $42.0°$. Powder diffraction files of the known equilibrium Li_xSi alloys (i.e., $Li_{22}Si_5$, $Li_{13}Si_4$, Li_7Si_3, and $Li_{12}Si_7$) show many similar features in this region, though none that directly correspond to these peaks. Instead, these peaks between $39°$ and $43°$ have been attributed to metastable ordered phases of lithium silicide[35] that occur due to the partially amorphous nature of the alloy

Figure 5. SEM images of Si wafers after (a), (d), (g) partial alloy; (b), (e), (h) full alloy; and (c), (f), (i) cycled alloy/dealloy. (a−c) Cross-sectional view; scale bar = 50 μm. (d−f) 30° tilt view; scale bar = 100 μm. (g−i) Top-down view; scale bar = 100 μm.

and which, when present in a sample concurrently, will produce a spectra similar to that of Figure 4.[36]

3.3. Fracture Analysis. As shown in Figure 5, lithiation of a silicon coupon at 250 °C leads to numerous cracks appearing in the Li$_x$Si layer after the first lithiation step (regardless of whether the Si coupon is partially or fully alloyed), contrary to other reported observations.[9,13] While this is not expected for bulk silicon during lithiation, given the findings in previous studies, it is far from a unique phenomenon. For example, lithiation of crystalline Si nanoparticles and nanowires involves a curved two-phase boundary, i.e., core−shell interface, where the excessive tensile hoop stress can trigger morphological instability and fracture in the lithiated shell.[37,38] Additionally, Lee et al. reported that the fracture locations in lithiated Si nanopillars could be correlated to the highly anisotropic nature of the lithium insertion into Si and the resulting nonuniform electrode expansion.[39] Amorphous Si thin-film electrodes also exhibit crack development during the initial lithiation due to a high tensile stress generated by bending of the lithium−Si subsurface layer.[40] Note that regardless of the electrode shapes the stress state of the lithiated layer is always under tensile stress during delithiation, initiating new cracks or propagating existing microcracks.

The vertical cracks that appear in bulk silicon during alloying at 250 °C indicate that the Li$_x$Si layer was under tensile stress of a magnitude greater than the critical fracture energy of Li$_x$Si. These cracks can be seen in Figure 5(a), which shows the cross-sectional SEM images of a partially lithiated sample (8 × 10^4 s, 0.4 mA/cm^2) populated by through-thickness cracks perpendicular to the electrode surface. The source of the tensile stress responsible for crack development in the Li$_x$Si layer is currently unclear and may be related to the compounded effects of certain factors, such as a mismatch in

coefficients of thermal expansion between the Li$_x$Si layer and the underlying Si substrate, a high current density causing a more rapid volumetric expansion of the surface layer as alloying occurs, a loss of lithium by its reaction with moisture before/during the post-mortem analysis, an external pressure applied to the coupon within the Swagelok setup, etc. Verifying the dominant factor and determining other mechanisms that may play a role in crack development during the initial lithiation require more in-depth investigations and are subject to future work.

Upon further lithiation, i.e., when the Si electrode was alloyed until the half-cell voltage dropped below the cutoff voltage (0.01 V), the reaction front, or Li$_x$Si/Si phase boundary, moved deeper into the underlying Si electrode. Figure 5(b) shows the cross-sectional view of the fully alloyed (0.4 mA/cm^2, 0.01 V cutoff) Si coupon. The average thickness of the Li$_x$Si layer in the full alloy sample is 66.5 ± 4.1 μm, increased from the 57.4 ± 4.3 μm layer thickness of the partial alloy sample. While the lithiation duration approximately doubled from the partially alloyed state to the fully alloyed state, the Li$_x$Si layer thickness increased by only 16%. This result diverges from previous reports, in which the amorphous layer thickness is observed to increase linearly with the lithiation time (i.e., $L \propto t$).[12] The $L \propto t$ relation suggests that lithiation kinetics is regulated by short-range processes near the reaction front,[41] though these observations may only correspond to shallow lithiation cases in which the Li$_x$Si thickness is less than a few microns. In the lithiation study presented here, a practical, high-current-density alloy step was utilized, leading to an Li$_x$Si layer thickness of several tens of microns, where long-range diffusive transport of Li through the existing Li$_x$Si layer could be a rate-limiting step.[42]
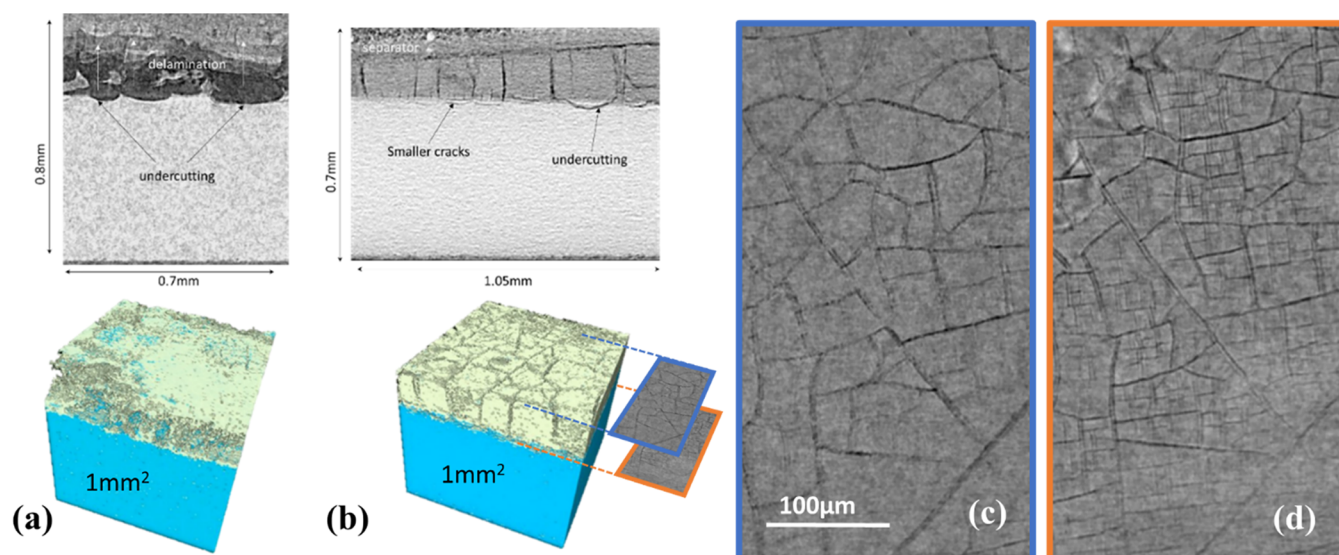
Figure 6. X-ray computed tomography 2D slices and 3D renderings of a (a) partial alloy and (b) full alloy. 2D images of a full alloy (c) at the surface of the Si wafer and (d) near the reaction front in the wafer.

The tilted SEM images in Figure 5(d−f) reveal that many of the major crack lines (wide, through-thickness) are orthogonal to the cleaved plane of Si. Considering the Si coupons used in this study are prepared from a (100) Si wafer and cleaved along and perpendicular to the major flat plane (⟨110⟩), these crack lines are roughly aligned to the ⟨110⟩ direction. These ⟨110⟩-oriented cracks may have been initiated from the ⟨110⟩-oriented buckles formed during the initial lithiation step.[13] Though these buckles were not observed in the SEM, it has been well documented that the lithiation rate is highest in the ⟨110⟩ direction of crystalline Si (c-Si),[39] and therefore it can be speculated that this anisotropic lithiation may cause ⟨110⟩-oriented buckling patterns during the initial lithiation step and eventually ⟨110⟩-oriented cracks when subjected to tensile stresses. Figure 5(g−i) also shows that some of the cracks occur in the ⟨100⟩ direction, which is consistent with previous reports[9,13] and can be explained by the linear elastic fracture mechanics of multilayer structures.[43] Briefly, the fracture behavior of the top layer (i.e., Li$_x$Si) is partly influenced by the mechanical properties of the underlying Si substrate. As c-Si has anisotropic mechanical properties and its ⟨100⟩ direction exhibits the smallest plane strain tensile modulus, the critical cracking thickness becomes smallest in that direction; i.e., the crack would preferentially propagate in the ⟨100⟩ direction.[13]

In addition to cracking in the ⟨110⟩ direction, there was also lateral cracking observed near the reaction (lithiation) front. This lateral cracking, also called undercutting due to the cracks occurring beneath the Li$_x$Si layer, causes the top layer to become mechanically unstable and prone to delamination; this is one of the major contributing issues in pulverization of the Si electrode. Whereas some of these cracks are visible in the SEM images, X-ray computed tomography (CT) is a better method to study lateral cracking in these Li alloyed Si coupons. Figure 6 shows micro-CT 3D renderings of partial alloy and full alloy Si coupons and 2D slices of horizontal planes to detail differing cracking patterns at the top surface and near the reaction front.

The observations of a through-thickness scan of the micro-CT reveal that while fracture features on the surface appear large (Figure 6(c)) closer to the reaction front these features

become smaller (Figure 6(d)). This is presumably due to maximum volume expansion occurring at the fully lithiated surface, but incomplete lithiation at the reaction front results in a smaller volume expansion of the material and therefore more void space. With this technique, the degree and mode of fracturing can be studied without inducing additional stress from preparing the sample, as with other techniques.

The cross-sectional and tilted images of the Si electrode after alloy/dealloy are shown in Figure 5(c) and 5(f). The average thickness of the Li$_x$Si layer grew to 78.7 ± 2.4 μm, a substantial increase from the Li$_x$Si layer thickness in the full alloy sample. Additionally, the void space observed on the surface of the Si coupon, which correlates to the level of fracture, increased with the level of lithiation (seen in Table 2), as calculated by an ImageJ threshold analysis of the top-down SEM images shown in Figure 5(g−i).

Table 2. Comparison of the Li$_x$Si Layer Depth and Resulting Void Space in Si Coupon Electrodes

sample	Li$_x$Si layer depth (μm)	% of surface occupied by void (cracking)
partial alloy	57.4 ± 4.3	21.26%
full alloy	66.5 ± 4.1	23.40%
alloy/dealloy	78.7 ± 2.4	26.19%

An increasing trend in the lithiated layer thickness with continued cycling was demonstrated previously, though at a much lower current density.[9] Another feature of the sample that has been subjected to both alloying and dealloying is that a significant portion of the Li$_x$Si layer was absent, apparently delaminated during the alloy/dealloy process. In the remaining Li$_x$Si layer, the lateral cracks that lead to undercutting and, subsequently, delamination are clearly visible at the Li$_x$Si/Si interfaces, demonstrated in Figure 5(f). It is, however, important to note that the lithiation depth (or the thickness of the Li$_x$Si layer) in these experiments is an order of magnitude higher than the past works where a loss of the Si electrode by delamination was observed at a much shallower lithiation depth.

CONCLUSION

This study has successfully constructed and thermally activated a high-temperature (250 °C) electrochemical cell with molten LiTFSI electrolyte to study the effects of Li alloying and dealloying of a carbon-free bulk, flat Si electrode. SEM and CT analyses show that cracking occurs during lithiation in this study, although many previous reports claim that the dealloy process is the main cause of fracture. The reason for this discrepancy remains unclear, but it is likely due to a combination of the elevated temperature, as well as a current density much greater than those examined in previous studies, which subsequently caused a more rapid volumetric expansion of the surface layer on top of the bulk of unreacted Si. This rapid expansion created a mechanical strain in the brittle Si material, likely instigating the cracking. Additionally, whereas previous studies have reported a linear relationship between the thickness of the reacted layer and the alloying time, here this relationship breaks down, suggesting a different mode of lithiation kinetics when under high current and high-temperature conditions. These conditions produce a semiordered lithium silicide phase at 250 °C, as supported in the XRD of the alloyed and dealloyed materials, though it is evident that the formation of fully crystalline materials is not favored at this temperature.

In this work, we have begun to understand the process of Li/Si alloying at high temperatures, and there is much more work to be done to appreciate the implications of these results on high-temperature Li storage. Though the higher temperatures do not completely mitigate the pulverization of Si upon alloying/dealloying with lithium, this study has provided essential insights into the formation of these fracture features. Additional study at temperatures closer to 415 °C, under which conditions of lithiation of Si may form crystalline materials, will help us to further understand the fundamental interactions of Li and Si at elevated temperatures.

ASSOCIATED CONTENT

Supporting Information

The Supporting Information is available free of charge at https://pubs.acs.org/doi/10.1021/acsomega.2c01145.

Differential capacity analysis (dQ/dV) of electrochemical alloying and dealloying and powder diffraction files of known lithium silicides (PDF)

AUTHOR INFORMATION

Corresponding Author

Corey T. Love — *Chemistry Division, U.S. Naval Research Laboratory, SW Washington, DC 20375, United States;* orcid.org/0000-0003-2581-3625; Email: corey.love@nrl.navy.mil

Authors

Matthew J. Lefler — *NRL/NRC Post-doctoral Associate and Chemistry Division, U.S. Naval Research Laboratory, SW Washington, DC 20375, United States*

Junghoon Yeom — *Materials Science and Technology Division, U.S. Naval Research Laboratory, SW Washington, DC 20375, United States;* orcid.org/0000-0002-8671-2708

Christopher Rudolf — *Materials Science and Technology Division, U.S. Naval Research Laboratory, SW Washington, DC 20375, United States*

Rachel E. Carter — *Chemistry Division, U.S. Naval Research Laboratory, SW Washington, DC 20375, United States;* orcid.org/0000-0001-6583-1049

Complete contact information is available at:
https://pubs.acs.org/10.1021/acsomega.2c01145

Notes

The authors declare no competing financial interest.

ACKNOWLEDGMENTS

REFERENCES

(1) Bresser, D.; Paillard, E.; Passerini, S. Chapter 7 - Lithium-ion batteries (LIBs) for medium- and large-scale energy storage: emerging cell materials and components. In *Advances in Batteries for Medium and Large-Scale Energy Storage*; Menictas, C., Skyllas-Kazacos, M., Lim, T. M., Eds.; Woodhead Publishing, 2015; pp 213−289.

(2) Asenbauer, J.; Eisenmann, T.; Kuenzel, M.; Kazzazi, A.; Chen, Z.; Bresser, D. The success story of graphite as a lithium-ion anode material - fundamentals, remaining challenges, and recent developments including silicon (oxide) composites. *Sustainable Energy & Fuels* 2020, 4 (11), 5387−5416.

(3) Seefurth, R. N.; Sharma, R. A. Investigation of Lithium Utilization from A Lithium-Silicon Electrode. *J. Electrochem. Soc.* 1977, 124 (8), 1207−1214.

(4) Lai, S. C. Solid Lithium-Silicon Electrode. *J. Electrochem. Soc.* 1976, 123 (8), 1196−1197.

(5) Obrovac, M. N.; Chevrier, V. L. Alloy Negative Electrodes for Li-Ion Batteries. *Chem. Rev.* 2014, 114 (23), 11444−11502.

(6) Bresser, D.; Passerini, S.; Scrosati, B. Leveraging valuable synergies by combining alloying and conversion for lithium-ion anodes. *Energy Environ. Sci.* 2016, 9 (11), 3348−3367.

(7) Wen, C. J.; Huggins, R. A. Chemical diffusion in intermediate phases in the lithium-silicon system. *J. Solid State Chem.* 1981, 37 (3), 271−278.

(8) McDowell, M. T.; Lee, S. W.; Nix, W. D.; Cui, Y. 25th Anniversary Article: Understanding the Lithiation of Silicon and Other Alloying Anodes for Lithium-Ion Batteries. *Adv. Mater.* 2013, 25 (36), 4966−4985.

(9) Shi, F.; Song, Z.; Ross, P. N.; Somorjai, G. A.; Ritchie, R. O.; Komvopoulos, K. Failure mechanisms of single-crystal silicon electrodes in lithium-ion batteries. *Nat. Commun.* 2016, 7 (1), 11886.

(10) Ko, M.; Chae, S.; Cho, J. Challenges in Accommodating Volume Change of Si Anodes for Li-Ion Batteries. *ChemElectroChem.* 2015, 2 (11), 1645−1651.

(11) Zhao, H.; Yuan, W.; Liu, G. Hierarchical electrode design of high-capacity alloy nanomaterials for lithium-ion batteries. *Nano Today* 2015, 10 (2), 193−212.

(12) Chon, M. J.; Sethuraman, V. A.; McCormick, A.; Srinivasan, V.; Guduru, P. R. Real-Time Measurement of Stress and Damage Evolution during Initial Lithiation of Crystalline Silicon. *Phys. Rev. Lett.* 2011, 107 (4), 045503.

(13) Yoon, T.; Xiao, C.; Liu, J.; Wang, Y.; Son, S.; Burrell, A.; Ban, C. Electrochemically induced fractures in crystalline silicon anodes. *J. Power Sources* 2019, 425, 44−49.

(14) Eshetu, G. G.; Figgemeier, E. Confronting the Challenges of Next-Generation Silicon Anode-Based Lithium-Ion Batteries: Role of

Designer Electrolyte Additives and Polymeric Binders. *ChemSusChem* **2019**, *12* (12), 2515−2539.

(15) Wu, H.; Cui, Y. Designing nanostructured Si anodes for high energy lithium ion batteries. *Nano Today* **2012**, *7* (5), 414−429.

(16) Domi, Y.; Usui, H.; Yamaguchi, K.; Yodoya, S.; Sakaguchi, H. Silicon-Based Anodes with Long Cycle Life for Lithium-Ion Batteries Achieved by Significant Suppression of Their Volume Expansion in Ionic-Liquid Electrolyte. *ACS Appl. Mater. Interfaces* **2019**, *11* (3), 2950−2960.

(17) Chae, S.; Kwak, W.-J.; Han, K. S.; Li, S.; Engelhard, M. H.; Hu, J.; Wang, C.; Li, X.; Zhang, J.-G. Rational Design of Electrolytes for Long-Term Cycling of Si Anodes over a Wide Temperature Range. *ACS Energy Lett.* **2021**, *6* (2), 387−394.

(18) Choi, J. W.; Aurbach, D. Promise and reality of post-lithium-ion batteries with high energy densities. *Nat. Rev. Mater.* **2016**, *1* (4), 16013.

(19) Schall, J. D.; Gao, G.; Harrison, J. A. Elastic constants of silicon materials calculated as a function of temperature using a parametrization of the second-generation reactive empirical bond-order potential. *Phys. Rev. B* **2008**, *77* (11), 115209.

(20) Muñoz-Rojas, D.; Leriche, J.-B.; Delacourt, C.; Poizot, P.; Palacín, M. R.; Tarascon, J.-M. Development and implementation of a high temperature electrochemical cell for lithium batteries. *Electrochem. Commun.* **2007**, *9* (4), 708−712.

(21) Kerner, M.; Plylahan, N.; Scheers, J.; Johansson, P. Thermal stability and decomposition of lithium bis(fluorosulfonyl)imide (LiFSI) salts. *RCS Adv.* **2016**, *6* (28), 23327−23334.

(22) Ababtain, K.; Babu, G.; Lin, X.; Rodrigues, M.-T. F.; Gullapalli, H.; Ajayan, P. M.; Grinstaff, M. W.; Arava, L. M. R. Ionic Liquid-Organic Carbonate Electrolyte Blends To Stabilize Silicon Electrodes for Extending Lithium Ion Battery Operability to 100 °C. *ACS Appl. Mater. Interfaces* **2016**, *8* (24), 15242−15249.

(23) Rodrigues, M.-T. F.; Babu, G.; Gullapalli, H.; Kalaga, K.; Sayed, F. N.; Kato, K.; Joyner, J.; Ajayan, P. M. A materials perspective on Li-ion batteries at extreme temperatures. *Nat. Energy* **2017**, *2* (8), 17108.

(24) Salpekar, D.; Puthirath, A. B.; Hou, G.; Dharmarajan, B.; Ganguli, B.; Ajayan, P. M. An electrolyte with lithium dendrites suppression for high temperature operability. *Appl. Mater. Today* **2021**, *24*, 101087.

(25) Kubota, K.; Matsumoto, H. Investigation of an Intermediate Temperature Molten Lithium Salt Based on Fluorosulfonyl-(trifluoromethylsulfonyl)amide as a Solvent-Free Lithium Battery Electrolyte. *J. Phys. Chem. C* **2013**, *117* (37), 18829−18836.

(26) Choi, M.; Kim, J.-C.; Kim, D.-W. Waste Windshield-Derived Silicon/Carbon Nanocomposites as High-Performance Lithium-Ion Battery Anodes. *Sci. Rep.* **2018**, DOI: 10.1038/s41598-018-19529-1.

(27) Zhong, L.; Guo, J.; Mangolini, L. A stable silicon anode based on the uniform dispersion of quantum dots in a polymer matrix. *J. Power Sources* **2015**, *273*, 638−644.

(28) Wu, J. J.; Bennett, W. R. Fundamental investigation of Si anode in Li-Ion cells. *2012 IEEE Energytech* **2012**, 1−5.

(29) Jerliu, B.; Hüger, E.; Dörrer, L.; Seidlhofer, B. K.; Steitz, R.; Horisberger, M.; Schmidt, H. Lithium insertion into silicon electrodes studied by cyclic voltammetry and operando neutron reflectometry. *Phys. Chem. Chem. Phys.* **2018**, *20* (36), 23480−23491.

(30) Das, S.; Kashyap, N.; Kalita, S.; Bora, D. B.; Borah, R. Chapter One - A brief insight into the physicochemical properties of room-temperature acidic ionic liquids and their catalytic applications in CC bond formation reactions. In *Adv. Phys. Org. Chem.*; Williams, I. H., Williams, N. H., Eds.; Academic Press, 2020; Vol. *54*, pp 1−98.

(31) Principles of X-ray Diffraction. In *Thin Film Analysis by X-Ray Scattering*, Wiley: New York, 2005; pp 1−40.

(32) Zaumseil, P. High-resolution characterization of the forbidden Si 200 and Si 222 reflections. *J. Appl. Crystallogr.* **2015**, *48*, 528−532.

(33) Zhao, L.; Steinhart, M.; Yosef, M.; Lee, S. K.; Geppert, T.; Pippel, E.; Scholz, R.; Gösele, U.; Schlecht, S. Lithium Niobate Microtubes within Ordered Macroporous Silicon by Templated Thermolysis of a Single Source Precursor. *Chem. Mater.* **2005**, *17* (1), 3−5.

(34) Richard, M. I.; Metzger, T. H.; Holý, V.; Nordlund, K. Defect Cores Investigated by X-Ray Scattering close to Forbidden Reflections in Silicon. *Phys. Rev. Lett.* **2007**, *99* (22), 225504.

(35) Limthongkul, P.; Jang, Y.-I.; Dudney, N. J.; Chiang, Y.-M. Electrochemically-driven solid-state amorphization in lithium-silicon alloys and implications for lithium storage. *Acta Mater.* **2003**, *51* (4), 1103−1113.

(36) Doh, C.-H.; Oh, M.-W.; Han, B.-C. Lithium Alloying Potentials of Silicon as Anode of Lithium Secondary Batteries. *Asian J. Chem.* **2013**, *25* (10), 5739−5743.

(37) Ryu, I.; Choi, J. W.; Cui, Y.; Nix, W. D. Size-dependent fracture of Si nanowire battery anodes. *J. Mech. Phys. Solids* **2011**, *59* (9), 1717−1730.

(38) Huang, S.; Fan, F.; Li, J.; Zhang, S.; Zhu, T. Stress generation during lithiation of high-capacity electrode particles in lithium ion batteries. *Acta Mater.* **2013**, *61* (12), 4354−4364.

(39) Lee, S. W.; McDowell, M. T.; Choi, J. W.; Cui, Y. Anomalous Shape Changes of Silicon Nanopillars by Electrochemical Lithiation. *Nano Lett.* **2011**, *11* (7), 3034−3039.

(40) Chew, H. B.; Hou, B.; Wang, X.; Xia, S. Cracking mechanisms in lithiated silicon thin film electrodes. *Int. J. Solids Struct.* **2014**, *51* (23), 4176−4187.

(41) Liu, X. H.; Zheng, H.; Zhong, L.; Huang, S.; Karki, K.; Zhang, L. Q.; Liu, Y.; Kushima, A.; Liang, W. T.; Wang, J. W.; et al. Anisotropic Swelling and Fracture of Silicon Nanowires during Lithiation. *Nano Lett.* **2011**, *11* (8), 3312−3318.

(42) Choi, Y.-S.; Scanlon, D. O.; Lee, J.-C. Extending the Performance Limit of Anodes: Insights from Diffusion Kinetics of Alloying Anodes. *Adv. Energy Mater.* **2021**, *11* (27), 2003078.

(43) Hutchinson, J. W.; Suo, Z. Mixed Mode Cracking in Layered Materials. In *Advances in Applied Mechanics*; Hutchinson, J. W., Wu, T. Y., Eds.; Elsevier, 1991; Vol. *29*, pp 63−191.